



Effects of large strain reverse loading on the strain rate dependence and dynamic strain localization of ductile metallic rods

Longhui Zhang · David Townsend

Received: 8 April 2022 / Accepted: 3 November 2022 / Published online: 24 November 2022
© The Author(s) 2022

Abstract The dynamic necking of ductile metallic rods with large strain reverse loading history has received little attention in the published literature. A novel bespoke real time strain control setup is constructed to apply the reverse loading directly to the specimen gauge section up to a maximum strain level of ± 0.16 . 304L stainless steel is used as a model material in this study. The subsequent tensile tests of the reverse loaded specimens are performed from quasi-static to high strain rates of 1000/s, using a Zwick 050 Machine, hydraulic Instron 8854, and a bespoke split Hopkinson tension bar with high speed photography equipment. The initial flow stress of the 304L rods shows similar strain rate dependence, regardless of the reverse loading history. The local strain rate during strain localization increases dramatically and eventually reaches one order of magnitude higher than the nominal strain rate. A higher strain reverse loading significantly influences the development of necking instabilities, with smaller strain to necking inception, higher local stress in the necking zone, and higher local strain rate up to failure. Instead of evaluating the impact energy absorption up to necking, an analysis of the local stress–strain relationship indicates that the reverse loaded 304L shows

good impact energy absorption up to failure. This agrees with the ductile fracture surfaces of the 304L materials with reverse loading.

Keywords Reverse loading · Ductile rod · Hopkinson bar · Dynamic necking · Energy absorption

1 Introduction

The engineering materials used in practical structures are inevitably subjected to impact loading. It's important to evaluate the energy absorption of the materials. The mechanical behavior of metallic alloys is influenced by a series of parameters, such as strain rate (and temperature) in the monotonic loading process up to failure [1–5]. However, the properties of the initial materials in the test would be not the same as those in service. Likewise, the test condition would not meet the service condition. The mechanical property of materials would be weakened by the cycle loading. In the manufacturing process or service, the cycle loading is unavoidable. It is important to study the mechanical response of materials after cycle loading.

As suggested by Pinnola and Franchi et al. [6, 7], it is important to accurately characterize the stress–strain relation to understand the tensile behavior of metals during forming and machining processes. The tensile property can be altered

L. Zhang (✉) · D. Townsend
Department of Engineering Science, University of Oxford,
Parks Road, Oxford OX1 3PJ, UK
e-mail: longhui.zhang@eng.ox.ac.uk;
lh Zhang.mechanics@gmail.com

through reverse loading, which depends on the microstructure, the number of cycles and the amplitude of the cycle. In addition, the influence of reverse loading on the tensile behavior would be different at quasi-static loading and high strain rate loading. After being subjected to reverse loading, the tensile properties of some materials, such as steel [8–10] and nickel alloy [11], change significantly at different strain rates. However, the influence of cycle loading is not significant for Al alloys [12, 13] and Titanium alloy [14] at both quasi-static and high strain rates. Despite the great interest in the mechanical properties of metals with cycle loading history, most of the available studies focused on the cyclic behavior at a relatively small strain of less than 0.1. Due to the difficulties in the strain control and the issue of specimen alignment, the effect of large strain cycle loading on the mechanical behavior of material is rarely reported in the literature. It is worthwhile to investigate the effect of large-strain reverse loading on the flow and failure of metals [15, 16].

Tensile test of alloys is associated with necking beyond a maximum load and the strain localization with a decreasing force [17–21]. Application of materials at high speed deformation requires the understanding of the dynamic strain localization. The tensile tests at high strain rates can be performed using the Split Hopkinson tension bar (SHTB) technique developed by Harding et al. [22, 23]. With the use of high speed photography techniques, the deformation and geometry change of the specimen can be monitored to study dynamic strain localization, see Noble et al. [24], Mirone et al. [25, 26] and Cadoni [27]. As a powerful full field measurement technique with non-contact characteristics, Digital Image Correlation (DIC) [28–30] provides a direct strain measurement of the specimen gauge section. However, limited effort has been made to monitor the dynamic strain localization of materials with reverse loading history in the literature. Likewise, studies concerning energy absorption of materials with reverse loading history are rarely reported, which require the measurement of the local stress–strain behavior in the necking zone using the high speed photograph techniques. The SHTB apparatus complemented by high speed DIC technique offers an opportunity to investigate the dynamic constitutive response and strain localization of alloys with reverse loading history.

In the aerospace industry, there is an increasing demand in reducing weight and fuel consumption. This requires novel design solutions and improved analytical methods to reduce the time and cost at the development stage. The containment casing [31] surrounding the fan blades contributes significantly to the overall weight of a modern aero engine. The containment component in the manufacturing process and in service would be subjected to reverse loading [32, 33]. Stainless steels with the combination of high strength/weight ratio and outstanding resistance to corrosion are important in the jet engine containment application [34]. Lee et al. [35, 36] reported that the impact behavior of the 304L stainless steel was affected by the previous deformation history. Rao et al. [37] investigated the prior cold work effect on the low-cycle fatigue behavior of the 304L. Iino [38] reported that the pre-strain reduced the yield strength of the pre-strained 304L. Hamasaki et al. [16] evaluated the stress–strain curves and the microstructure evolution under quasi-isothermal monotonic and cyclic loading condition. In the literature, the dynamic constitutive response and strain localization of the 304L with reverse loading history are missing. The understanding of the influence of reverse loading on the subsequent impact resistance and energy absorption is of considerable interest to the engineering and material communities. The present work has the following three goals:

- Designing a novel experimental technique for large strain reverse loading, with real time feedback of the strain of the specimen gauge section to control the applied reverse loading.
- Studying the Bauschinger effect of 304L, and the constitutive behavior of 304L with large strain reverse loading and its strain rate dependence.
- Investigating the influence of large strain reverse loading on the development of dynamic necking instabilities, and dynamic energy absorption of 304L with large strain reverse loading.

Therefore, in this paper, the material, the specimen design and the bespoke reverse loading technique are introduced in Sect. 2. The results across various strain rates are presented in Sect. 3. Section 4 discusses the outcome of this work, followed by the conclusions.

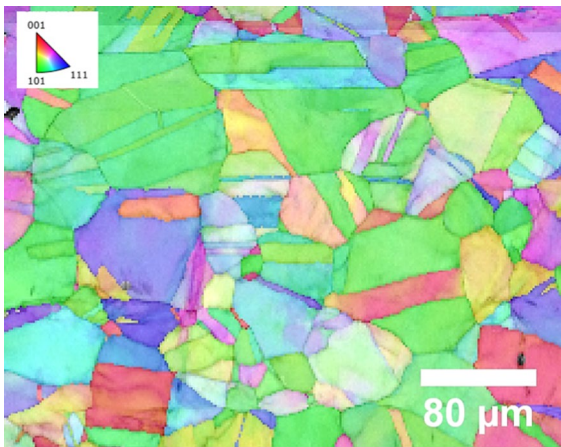


Fig. 1 As-received microstructure of the 304L from EBSD orientation map

2 Experimental protocol

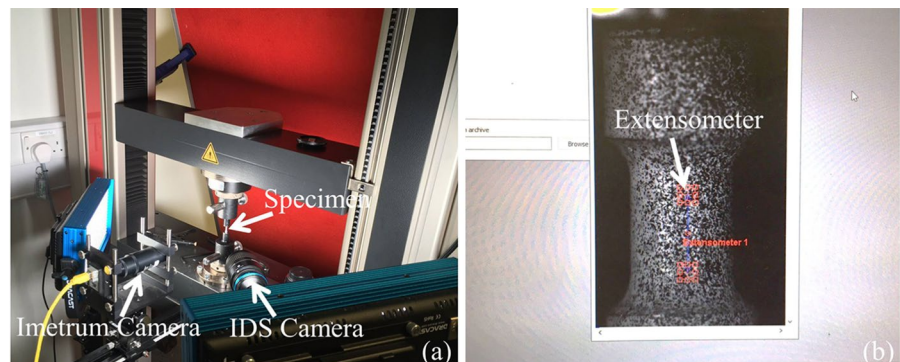
2.1 Material

A commercial 304L stainless steel, supplied from Smiths Metal Centres Ltd., was used as a model material in the present work. After being grinded and polished by colloidal silica suspension, the microstructure of the as-received 304L was revealed by EBSD using Zeiss EVO 15LS Scanning Electron Microscope. The microstructure of the as-received

Table 1 Chemical composition of the 304L stainless steel

C	Cr	Mn	Si	P	S	Ni	Fe
0.07	18.00	2.00	1.00	0.05	0.02	8.00	Bal

Fig. 2 Experimental setup for reverse loading with real time strain control **a** Image of the experimental setup. **b** Typical view from Imetrum system



304L from EBSD orientation map is shown in Fig. 1, which consists of grains with an average size of about 24 μm. The chemical compositions of the 304L from the supplier are given in Table 1.

2.2 Reverse loading methodology and specimen design

The reverse loading tests were conducted using a Zwick Z050 machine under displacement control mode at nominal strain rate of 0.01/s. As shown in Fig. 2a, the reverse loading was monitored by an Imetrum video extensometer¹ at a frame rate of 10 fps. This system tracks the engineering strain from an extensometer positioned across the gauge length of dog-bone specimen. The Imetrum system was programmed to provide feedback to the Zwick Z050 machine, in order to apply the reverse loading to the tensile specimen with a direct strain control.

A short gauge length specimen is desirable to avoid the misalignment of the specimen during the reverse loading process. A tensile specimen with a gauge length to diameter ratio of 3–3 mm was designed. Figure 2b shows a typical view of the specimen from the Imetrum system, with a marked extensometer in the gauge section for a real time measurement of engineering strain.

Figure 3 shows the geometry of specimen, which was manufactured along the axis direction from the

¹ Imetrum Limited, The Courtyard, Wraxall, Bristol, BS48 1NA, United Kingdom.

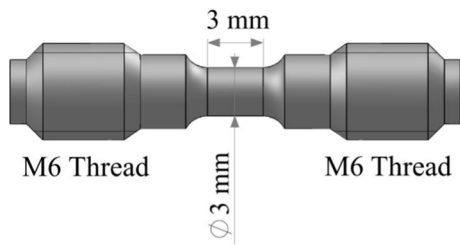


Fig. 3 Dimension of the specimen (unit: mm)

as-received material bar. The distribution of the triaxiality factor of the gauge section is evaluated in Fig. 21. The stress triaxiality at most of the gauge section is between 0.3 and 0.4. Furthermore, an 8 mm gauge length specimen was loaded at nominal strain rate of 0.01/s. Figure 4a shows that the stress–strain curve measured from the 3 mm gauge length specimen agrees with that measured from the 8 mm gauge length specimen. In addition, the 3 mm gauge length specimen was subjected to tensile loading at a lower strain rate of 0.0008/s.

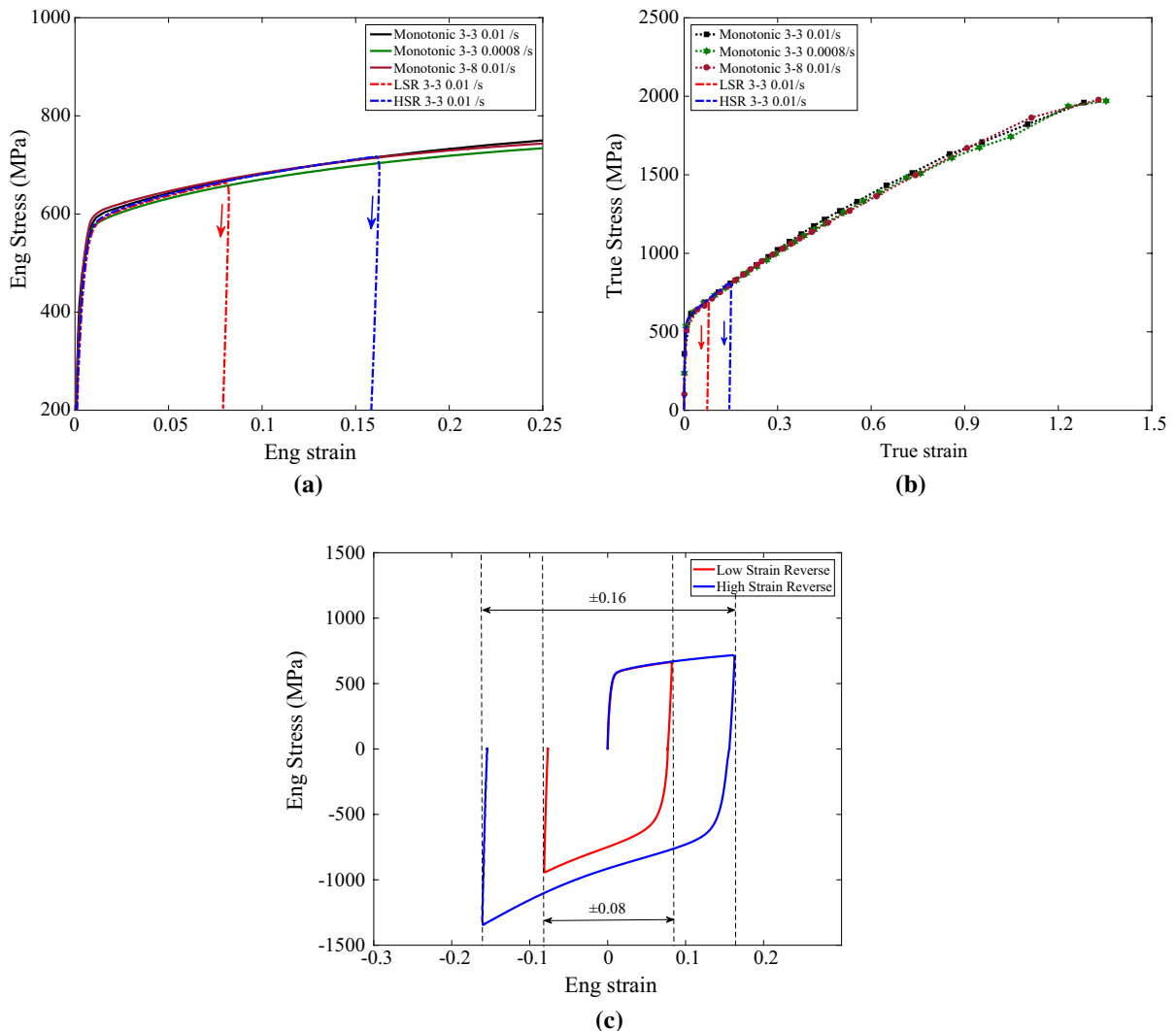


Fig. 4 **a** Comparison of the tensile engineering stress–strain curves measured from the 3 mm gauge length specimen and 8 mm gauge length specimen at the same strain rate of 0.01/s, and from the 3 mm gauge length specimen at a lower strain

rate of 0.0008/s. **b** The corresponding true stress–strain curves up to failure. **c** Engineering stress–strain curves during the tension–compression reverse loading process

Table 2 Equivalent plastic strain and grain size of 304L without and with reverse loading

Materials	Initial 304L	304L with LSR	304L with HSR
Equivalent plastic strain	0	0.23	0.45
Grain size (um)	24	18	8

Figure 4b compares the local true stress–strain relationships based on the Bridgman’s analysis [39]. The true stress–strain curves are plotted together up to failure, respectively obtained from the 3 mm gauge length specimen at nominal strain rate of 0.01/s and 0.0008/s, and the 8 mm gauge length specimen at nominal strain rate of 0.01/s. A modest strain rate effect can be seen, with a moderate difference of stress value about 10–20 MPa throughout the test duration up to failure. The consistent local stress–strain curves of different gauge length specimens agree with the recent analysis [25, 40].

For the low strain reverse (LSR) loading, when the tensile strain of gauge section reached +0.08, the specimen was unloaded. The unloaded specimen is immediately subjected to the reverse compressive loading up to a compressive strain of –0.08, followed by the unloading. The entire engineering stress–strain curve during this low strain reverse loading process is presented in Fig. 4c. Similarly, for the high strain reverse (HSR) loading, the tensile loading was applied up to a strain of +0.16 and the reverse compressive loading was applied up to a strain of –0.16. The maximum achievable strain in the tension–compression loading is 0.16. EBSD analysis revealed that the average grain size reduced from 24 um in the initial 304L to 18 um in the 304L with LSR loading, and to 8 um in the 304L with HSR loading. This is summarized in Table 2, together with the equivalent (accumulated) plastic strain. This is a common observation of grain size refinement during the reverse loading process [41, 42]. Here, instead of the multi-cycles reverse loading, only one cycle of tension–compression loading is considered to avoid any micro damages to the specimen [43–45]. This is important to measure the local stress–strain relationship of the specimens based on the volume constancy. After recovery, the reverse loaded specimens were tested from quasi-static to high strain rates.

2.3 Quasi-static test

The quasi-static tests up to fracture include the tests of the 304L specimens without reverse loading and with two strain levels of reverse loading. All tests were performed using a Zwick Z050 machine at nominal strain rate of 0.01/s. Likewise, the 3 mm length–3 mm diameter cylinders were compressively loaded at nominal strain rate of 0.01/s, in order to compare the monotonic compressive and tensile responses of the 304L material. The deformation was monitored by an IDS UEye 3.0 Camera with an image resolution of 2456×2054 pixels. The engineering strain of the specimen gauge section was analysed and measured by a commercial software LaVision Davis.²

2.4 Medium strain rate test

The tests at medium strain rate were carried out on a hydraulic Instron 8854 system. The load cell was programmed to apply the tensile loading to the specimens under displacement control corresponding to a nominal strain rate of 10/s. A phantom camera was employed to record the deformation of the specimen at a frame rate of 10,000 fps, with an image resolution of 512×512 pixels.

2.5 High strain rate tests

The tests at high strain rates of about 1000/s were conducted on a bespoke SHTB system [46, 47]. The incident bar and transmitted bar are 2.7 m in length and 16 mm in diameter. The incident bar was made from Ti6Al4V alloy and the transmitted bar was made from phosphor bronze. The dynamic deformation of the specimen was monitored by a high-speed camera (Kirana camera) with an image resolution of 924×748 pixels, at a frame rate of 200,000 fps. The schematic of the SHTB system is shown in Fig. 5. Specifically, one strain gauge was attached on the transmitted bar, and two strain gauges were on the incident bar. The pressure chamber with a piston connected to a pulling rod, allows the use of a 2.5 m long Ti6Al4V striker bar to test the 304L under large deformation. However, with such a long strike bar, the stress waves were

² LaVisionUK Ltd, 2 Minton Place Victoria Road, Bicester OX26 6QB, United Kingdom.

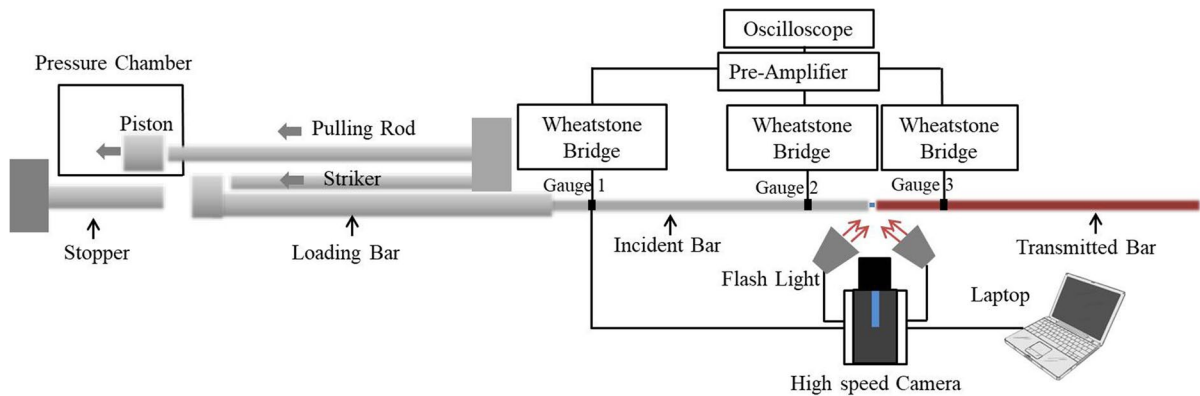


Fig. 5 Schematic of the SHTB system

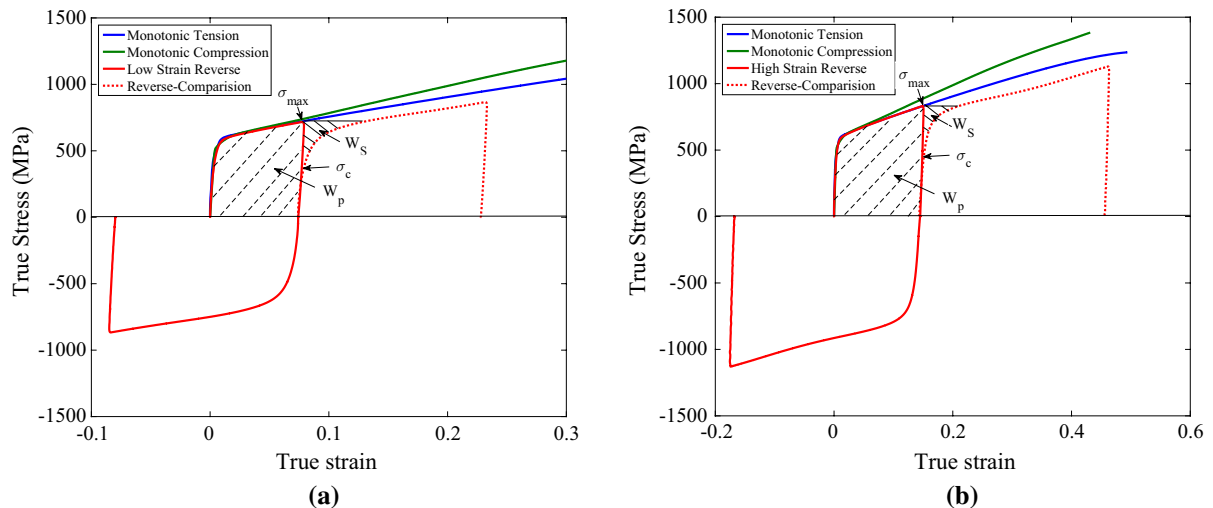


Fig. 6 Parameters to characterize the Bauschinger effect of the 304L material. **a** Low strain reverse loading. **b** High strain reverse loading

superimposed in the incident bar. Consequently, two strain gauges were attached to the incident bar to separate the superimposed waves.

3 Results

3.1 Quasi-static test results

3.1.1 Bauschinger effect in reverse loading

Figure 6 shows the typical true stress–strain curves of the 304L under two strain levels of reverse

loading measured by the Imetrum system, together with the average monotonic tensile and compressive stress–strain curves measured by the DIC. The true strain during the uniform deformation stage is transformed based on the volume constancy [48]. The yield stress of the monotonic compressive stress–strain curve is about 470 MPa. This is slightly lower than the yield stress 500 MPa of the monotonic tensile stress–strain curve. The strain hardening of the monotonic compressive stress–strain curve is more significant than that of the monotonic tensile stress–strain curve. Considering the reverse loading process, the stress–strain response of metals subjected

Table 3 Parameters of the Bauschinger effect indicators

Indicators	Low strain reverse	High strain reverse
β_σ	0.451	0.457
β_W	0.058	0.065
σ_{int}	164 MPa	190 MPa

to the reverse loading does not comply with the ideal plastic behavior, a subject firstly studied by Bauschinger [49]. At the beginning of reversal loading, an early yielding indicates the Bauschinger effect. A series of parameters [50] have been used to evaluate the Bauschinger effects. The parameters are displayed in Fig. 6. The compressive curve is mirrored in the tensile domain to simplify the definition of the Bauschinger effect indicators.

A reduced yield stress in the reverse compressive loading can be seen in Fig. 6, which indicates the Bauschinger effect of the 304L material. Except for a lower flow stress, the trends of the plastic flow and strain hardening during the compressive reverse loading are similar to those under monotonic tensile loading. The Bauschinger stress parameter β_σ , Bauschinger energy density parameter β_W and Bauschinger internal stress parameter σ_{int} are given by

$$\beta_\sigma = \frac{\sigma_{max} - \sigma_C}{\sigma_{max}} \tag{1}$$

$$\beta_W = \frac{W_S}{W_P} \tag{2}$$

$$\sigma_{int} = \frac{\sigma_{max} + \sigma_C}{2} \tag{3}$$

where σ_{max} is the maximum stress during the initial tensile loading, σ_C is the yield stress at the compression stage and is shown with a positive value here. W_S is the Bauschinger energy density and W_P is the pre-strain energy density. The parameters under two strain levels of reverse loading are listed in Table 3. The Bauschinger energy factor of 0.065 under HSR loading is higher than 0.058 under LSR loading. As a good indicator of the Bauschinger effect, the Bauschinger energy factor reflects the stress–strain relationship and the rapid strain hardening under HSR loading. The internal stress parameter describes the back stress. Table 3 shows that the Bauschinger stress

parameter increases from 164 MPa under LSR loading to 190 MPa under HSR loading. Consequently, the current setup can be used to reveal the Bauschinger effect of the 304L material.

3.1.2 Quasi-static tensile results

Figure 7 shows the quasi-static stress–strain relationships of the 304L without reverse loading, with LSR and HSR loading. According to Bridgman’s analysis [39], the local true stress and true strain at the center of necking can be calculated by:

$$\sigma_{true} = \frac{F}{\pi r^2} \tag{4}$$

$$\epsilon_{true} = 2 \ln \left(\frac{r_0}{r} \right) \tag{5}$$

here F is the instantaneous acting force, r is the current radius of the minimum cross-section of gauge section, r_0 is the initial radius of the gauge section. The change of radius can be obtained from the image analysis. For the initial 304L, the engineering stress–strain relation shows strain hardening up to a strain of 0.45, as can be seen in Fig. 7a. For the 304L with LSR loading, the engineering stress–strain relationship shows a yield stress of 660 MPa and strain hardening up to a necking strain of 0.4. The engineering stress–strain relationship of the 304L with HSR loading shows the highest yield stress of about 830 MPa and the peak stress of 980 MPa, followed by the necking. The engineering strain to failure of the 304L decreases with the reverse loading history. In Fig. 7b, the true stress–strain relation of the 304L with HSR loading shows the highest flow stress but lower strain hardening at a given true strain, compared to the initial 304L and the 304L with LSR loading. The true strain to failure decreases to about 1.1 for the 304L with HSR loading.

3.2 Medium strain rate test results

The tests at medium strain rate of 10/s were conducted, in order to evaluate the strain rate sensitivity of the 304L without reverse loading, with LSR and HSR loading. Figure 8a shows that the engineering stress–strain relationship of the initial 304L presents a yield stress of 560 MPa and strain hardening up to a

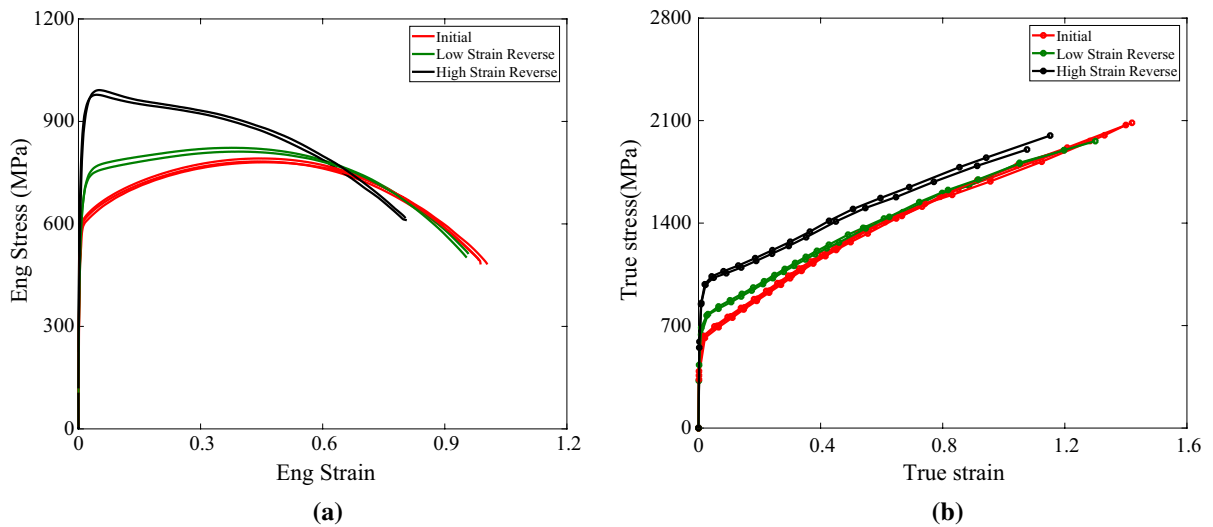


Fig. 7 Comparison of the quasi-static stress–strain relationships of the 304L without reverse loading, with LSR and HSR loading. **a** Engineering stress–strain, **b** true stress–strain

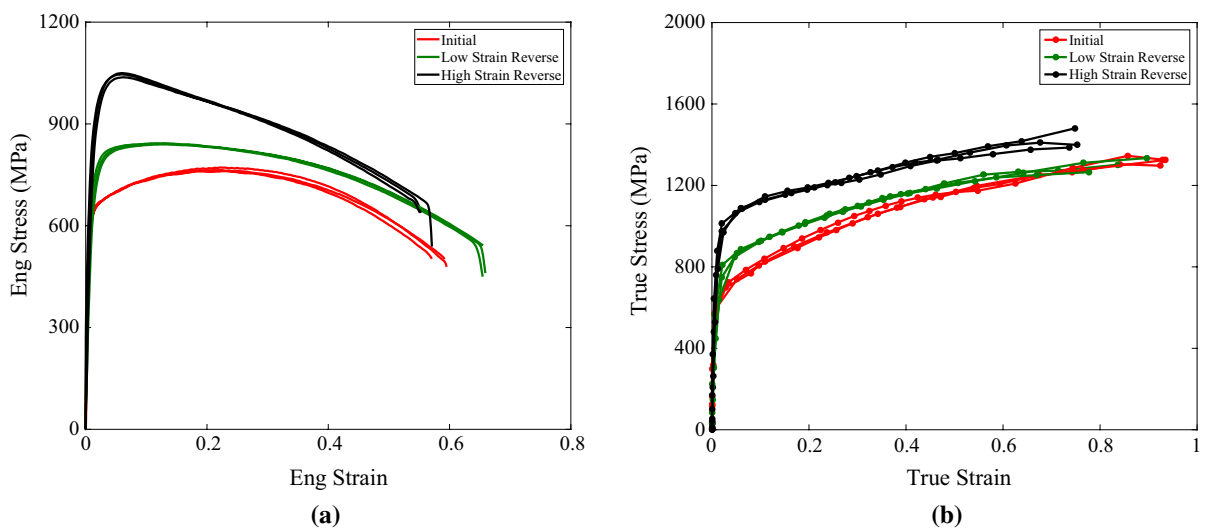


Fig. 8 Stress–strain relationships at medium strain rate of 10/s. **a** Engineering stress–strain and, **b** true stress–strain

strain of 0.24, followed by the necking. For the 304L with LSR and HSR loading, the yield stress values increase to 710 MPa and about 880 MPa respectively. The engineering stress–strain of the 304L with HSR loading shows the highest flow stress and the smallest strain to necking. For the initial 304L and the 304L

with HSR loading, the engineering failure strain values are of 0.6 and 0.5, respectively. For the 304L with LSR loading, the engineering failure strain slightly increases to 0.7. In Fig. 8b, the true stress–strain relationships of the reverse loaded 304L presents higher flow stress and lower strain hardening, compared to

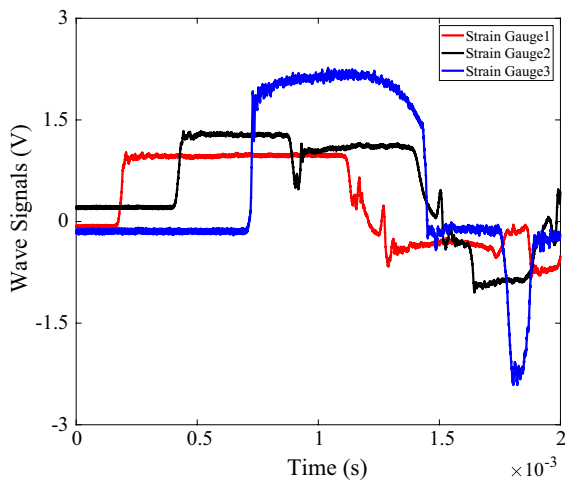


Fig. 9 Raw strain gauge signals of the initial 304L at high strain rate of 800/s

the initial 304L. The true strain to failure decreases to about 0.8 for the 304L with HSR loading.

3.3 High strain rate test results

The tests at high strain rate were performed on the SHTB system. Figure 9 shows the typical strain gauge signals. As mentioned in Sect. 2.5, the incident pulses are measured by two strain gauges (gauge 1 and 2) on the incident bar, and the transmitted pulse

is measured from the strain gauge (gauge 3) attached on the transmitted bar.

A valid SHTB test requires the force equilibrium at two ends of the specimen. Figure 10a shows that, after the initial stage when the stress wave transits through the 304L specimen, the input force agrees with the output force in the plastic region [51]. Similar force equilibrium can be seen in Fig. 10b for the 304L with HSR loading, which shows a higher force applied to the specimen, compared to the initial 304L.

Figure 11 shows the engineering stress and engineering strain evolutions at high strain rates, together with the corresponding axial engineering strain field from the DIC analysis. The engineering stress is measured by the output force from the SHTB analysis. The engineering strain is directly measured from the DIC analysis.

For the initial 304L, the engineering stress increases from stage 1 to stage 2 after the initial yield. This is followed by the necking at stage 3 and the fracture at stage 4. For the 304L with LSR loading, the dynamic flow stress is apparently higher than that of the initial 304L. However, the flow stress experiences almost no increase between stage 1 and stage 2. The necking localization appears at stage 3. The final fracture can be seen at stage 4. For the 304L with HSR loading, the flow stress firstly increases to 1125 MPa at the time of 150 μ s at stage 1, followed by the strain localization throughout most of the test duration. The engineering stress decreases at stage 2

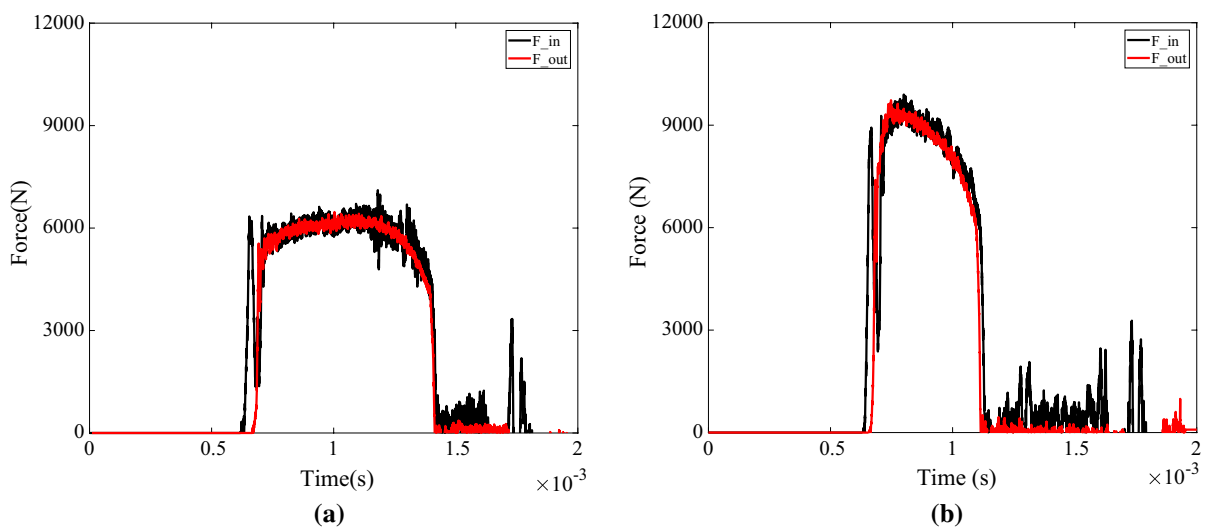


Fig. 10 Dynamic force equilibrium of (a) the initial 304L and (b) the 304L with HSR loading

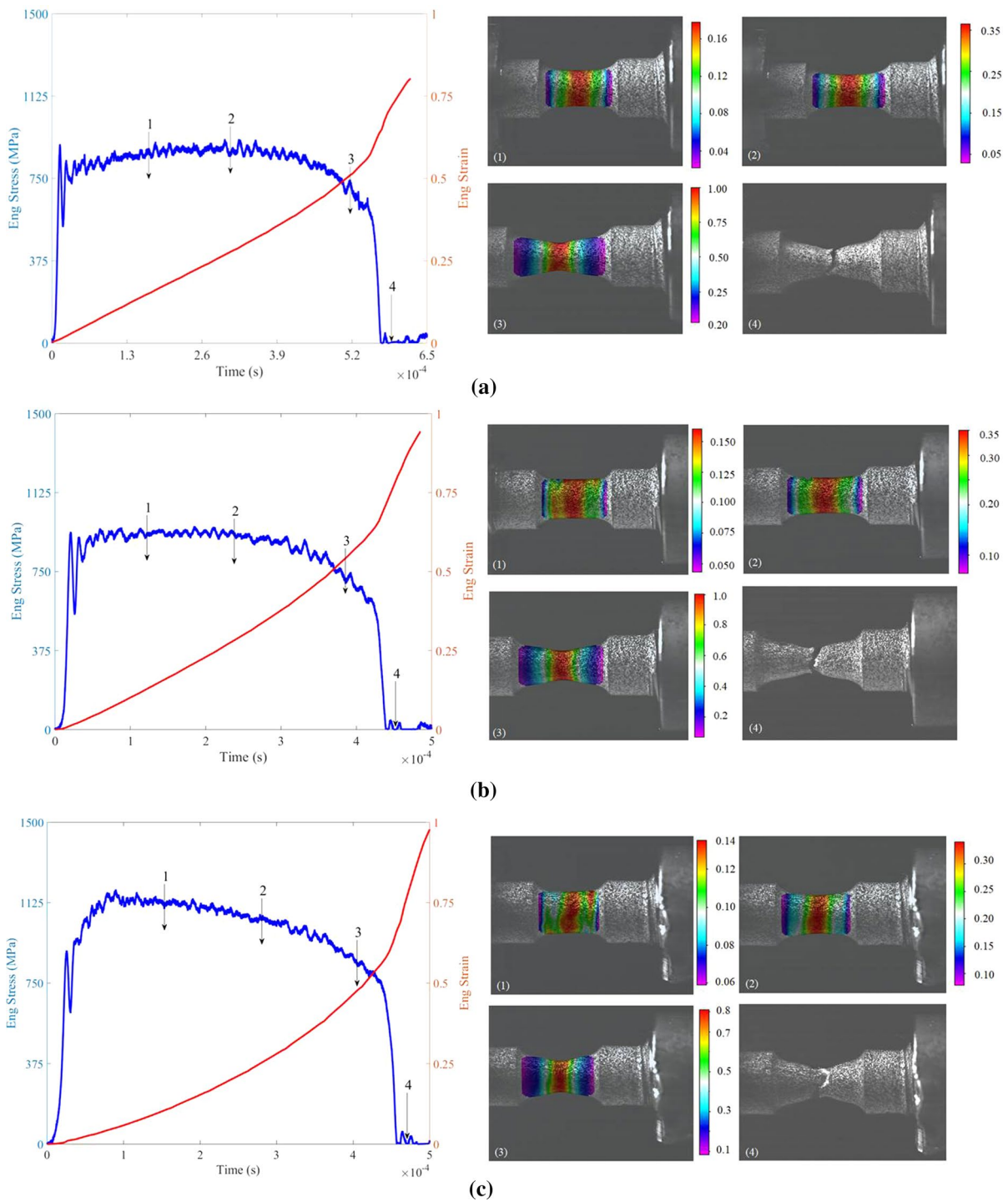


Fig. 11 Engineering stress and engineering strain histories, together with the DIC analysis of the axial engineering strain at different stages, for (a) the initial 304L (b) the 304L with LSR loading (c) the 304 with HSR loading

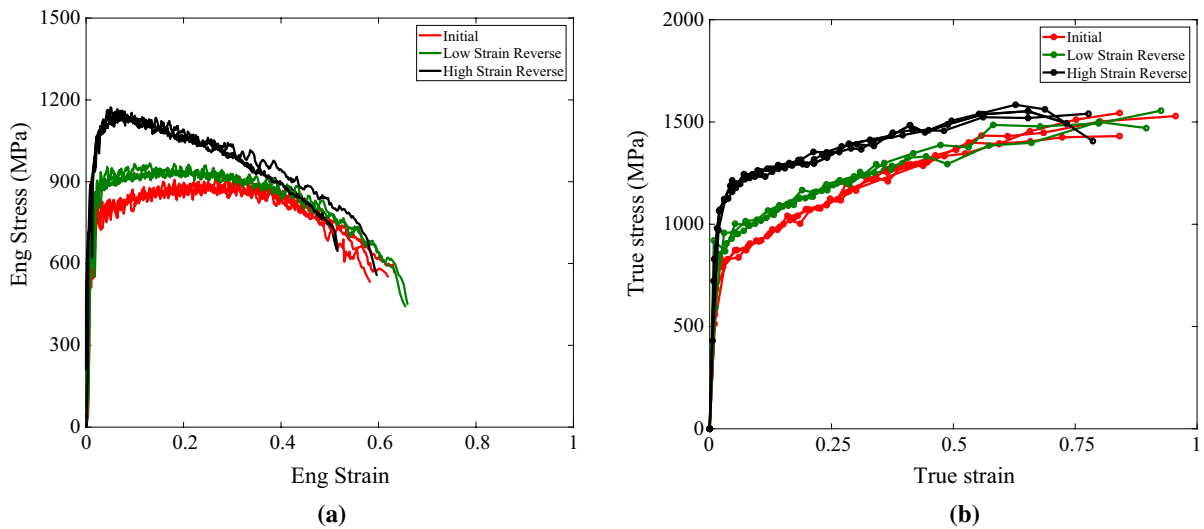


Fig. 12 Comparison of the dynamic **a** Engineering stress–strain relations, **b** True stress–strain relations of the 304L without reverse loading, with LSR and HSR loading

and stage 3 during strain localization, followed by the final fracture at stage 4.

Figure 12 compares the engineering and true stress–strain relationships at high strain rates for the 304L without reverse loading, with LSR and HSR loading. Figure 12a shows that the flow stress of the initial 304L presents apparent strain hardening until an engineering strain of about 0.35. For the 304L with LSR loading, the flow stress presents a mild strain hardening until an engineering strain of 0.3. The 304L materials without reverse loading and with LSR loading show a similar engineering strain to failure of 0.65. The 304L with HSR loading presents the highest yield and flow stress. The 304L with HSR loading shows necking at an engineering strain of 0.10.

To provide further insight into the necking localization, Fig. 12b compares the (local) true stress–strain relationships. The strain hardening of the 304L decreases with reverse loading history. The true stress–strain relationships of the 304L without reverse loading and with LSR loading are comparable beyond a true strain of 0.5, and show a true strain to failure of about 0.9. This is higher than the true strain to failure of 0.7, for the 304L with HSR loading.

Figure 13 summarizes the engineering stress–strain relationships of the 304L without reverse loading, with LSR and HSR loading. The yield stress of the

initial 304L increases from 500 MPa at quasi-static, 560 MPa at medium strain rate to 640 MPa at high strain rates of 700–1100/s. The engineering strain to failure decreases from 1 to 0.6 from quasi-static to high strain rates. For the 304L with LSR loading, the yield stress increases from 660 MPa from quasi-static to 800 MPa at high strain rates. The engineering strain to failure decreases from 1 to 0.6 from quasi-static to high strain rates. The 304L with HSR loading shows the highest yield stress of about 830 MPa at quasi-static and 960 MPa at high strain rates. The engineering strain to failure decreases to about 0.6 at high strain rates.

In order to evaluate the strain rate effect on the yield stress, Fig. 14 plots the engineering flow stress of the 304L materials as a function of nominal strain rate. Due to the difficulty in achieving the force equilibrium at the initial stage and in the determination of yield stress, the flow stress at a small strain of 0.05 is used instead of the yield stress. The 304L with HSR loading presents the highest flow stress values. The medium rate data is provided for a better understanding of the strain rate sensitivity. The Cowper–Symonds model [52] is used to reveal the flow stress as a function of strain rate, which is given by

$$\sigma = \sigma_{ref} \left[1 + \left(\frac{\dot{\epsilon}}{D} \right)^{\frac{1}{p}} \right] \tag{6}$$

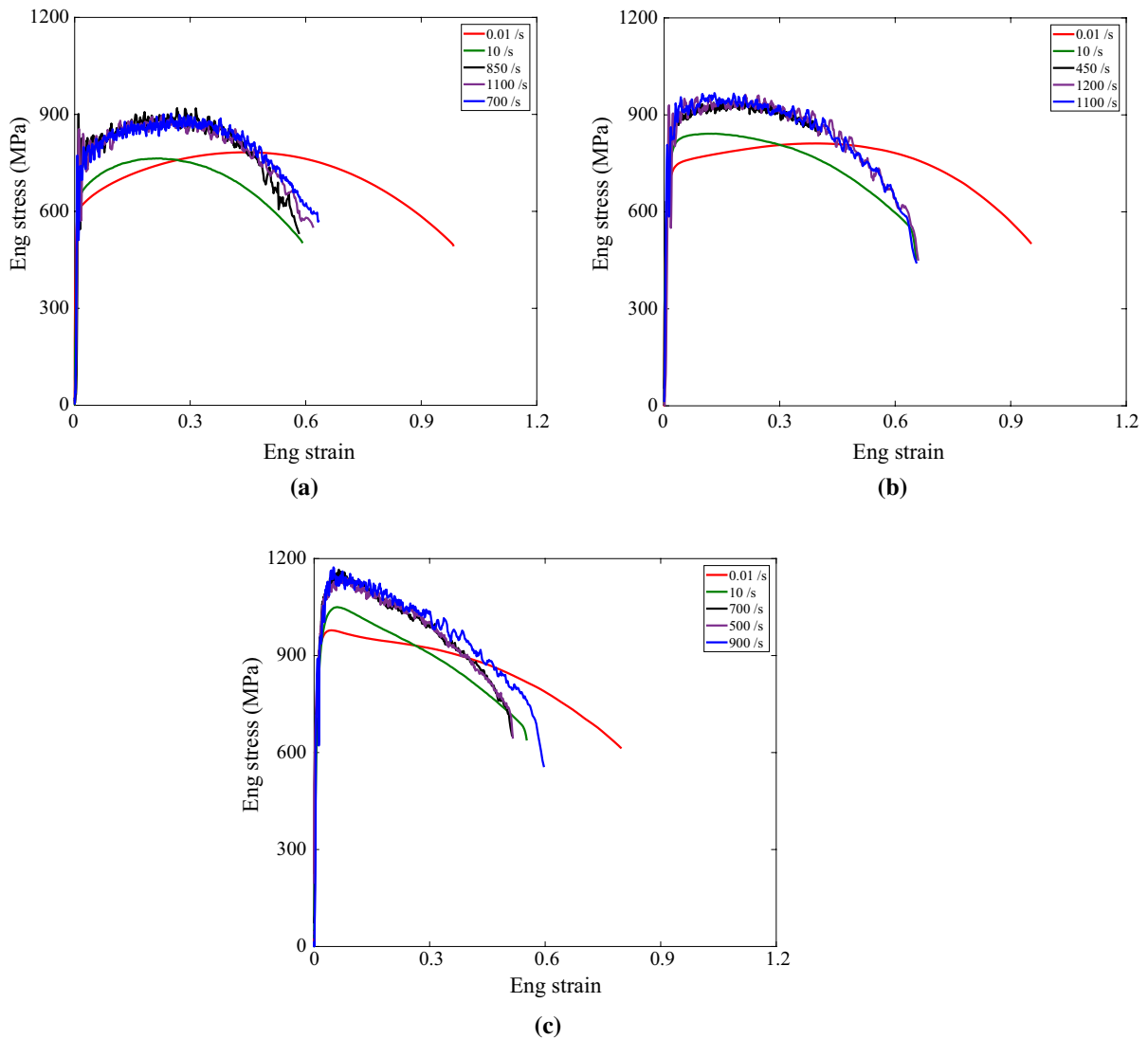


Fig. 13 The strain rate dependent engineering stress–strain relationships of the 304L **a** without reverse loading, **b** with LSR loading and **c** with HSR loading

where σ_{ref} is the reference flow stress at strain rate of 0.01/s, D and P are the strain rate dependence parameters. The calibrated constants are listed in Table 4. With a slight variation of the Cowper-Symonds model parameters, the 304L materials without reverse loading, with LSR and HSR loading show similar strain rate dependence.

Figure 15 compares the typical true stress–strain relations of the initial 304L and the 304L with LSR and HSR loading, to better highlight the strain rate sensitivity. The local stress across various strain rates is amplified in the 304L with reverse loading

history, compared to the initial 304L. In the range of the local strain from 0 to 0.30, the local flow stress increases significantly with increasing strain rate. Beyond the local strain of 0.30, the local flow stress values at medium and high strain rates are gradually smaller than that at static loading. The dynamic true strains to failure are lower than that under static condition, which can be observed in both of the initial and reverse loaded 304L. This indicates the flow and failure in the true stress–strain relation show apparent strain rate dependence.

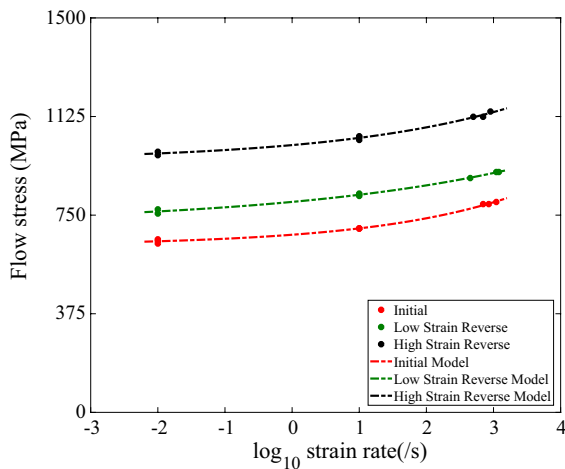


Fig. 14 Flow stress (close to the yield) versus strain rate of initial 304L and 304L with reverse loading

Table 4 Constants in the Cowper–Symonds model

Constants	<i>D</i>	<i>P</i>
Initial	8.358E5	4.9935
LSR	5.161E7	8.3783
HSR	2.310E7	6.1336

Due to the dynamic strain localization, the local true strain rate in the necking zone would be quite different from the nominal strain rate. The true strain rate at the time t_n can be determined by $\frac{e_{true}^n - e_{true}^{n-1}}{t_n - t_{n-1}}$, where e_{true}^n and e_{true}^{n-1} are the true strain at the time t_n and t_{n-1} , respectively. The time interval between the true strain measurements is 20 μ s. Figure 16 shows the typical local strain rate of the 304L without reverse loading, with LSR and HSR loading, at a comparable nominal strain rate of 900–1100/s. The true strain rate continues to increase rapidly, due to the strain localization. The local true strain rate reaches a value of one order of magnitude higher than the nominal strain rate. The 304L with HSR loading, which shows a longer duration of strain localization in Fig. 11, presents a higher local true strain rate at a given true strain.

Considering the dramatic increase of local strain rate, the ratio of dynamic true stress to static true stress (dynamic amplification) across different true strain and strain rate would be of interest. Figure 17a shows the dynamic amplification as a function of

local true strain for the 304L without reverse loading, with LSR and HSR loading respectively. A first observation is the decrease of dynamic amplification with the increase of true strain. This indicates the reduced work-hardening capacity of the 304L subjected to impact loading. The 304L with HSR loading shows an initial dynamic amplification factor of 1.15, which is slightly lower than the factor of 1.20 for the initial 304L and 304L with LSR. Likewise, Fig. 17b shows the dynamic amplification as a function of local strain rate. At comparable nominal strain rates, the dynamic amplification of the 304L with HSR decreases from 1.15 to 0.85. A similar decreasing trend can be seen for the initial 304L and the 304L with LSR. The decrease of the dynamic amplification with the increase of local strain rate indicates the strain rate promoted softening [53]. Likewise, this decreasing trend of the dynamic amplification would be associated with thermal softening due to the adiabatic self-heating [18]. This clearly shows that the surge of local strain rate does not immediately result in an increase in the local stress and the corresponding dynamic amplification.

Figure 18 compares the impact energy absorption of the 304L without reverse loading, with LSR and HSR loading. The energy density is calculated by $W = \int_0^\epsilon \sigma_{true} d\epsilon_{true}$. The energy density up to necking is shown in Fig. 18a, while the energy density up to fracture is given in Fig. 18b. Due to the early necking, the 304L with HSR loading shows the lowest impact energy absorption about 110 MJ/m³. This is much lower than the energy absorption of about 280 MJ/m³ for the initial 304L and the 304L with LSR loading, as can be seen in Fig. 18a. However, considering the energy absorption up fracture shown in Fig. 18b, the initial 304L and the 304L with LSR loading show a similar increase of the strain energy density, with the energy density at failure about 1100 MJ/m³. The 304L with HSR loading presents a more significant increase of the strain energy density at a given true strain. The strain energy density at failure for the 304L with HSR loading is about 1050 MJ/m³, which is only 5% lower than the 304L without reverse loading and with LSR loading. Although the HSR loading reduces the strain hardening and slightly reduces the true strain to failure, the impact energy absorption of the 304L can still be maintained.

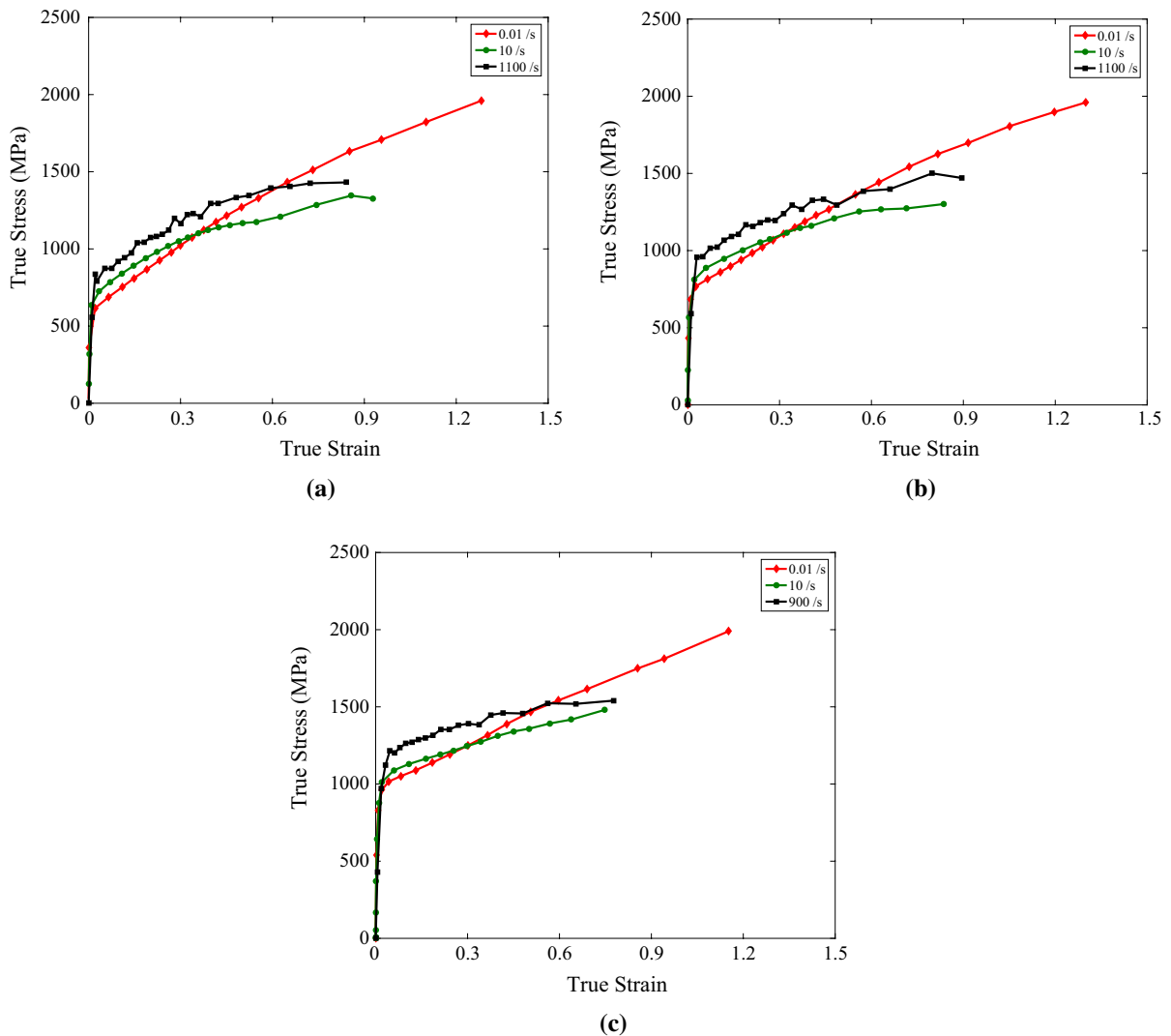


Fig. 15 The typical rate dependent true stress–strain relationships of the 304L **a** without reverse loading, **b** with LSR loading and **c** HSR loading

3.4 Microstructural characterization

The fracture surfaces of the dynamically failed 304L without reverse loading, with LSR loading and HSR loading are shown in Fig. 19. The micrographs on the edge of the cup fracture surface are listed on the left column, and the micrographs taken from the bottom of the cup fracture surface are shown on the right column.

The 304L without reverse loading consists of shear dimples (arrowed), relatively flat and smeared regions (circles in Fig. 19a, b), indicating a failure mode

associated with grain boundary sliding [54]. For the 304L with LSR loading, the fracture surface shows a region with shear elongated dimples (marked by an arrow in Fig. 19c). Figure 19d consists of a mixture of shallow dimples and deep circular voids. This indicates a good ductility of the 304L with low strain reverse loading [55, 56]. For the 304L with HSR loading, the fracture morphology in Fig. 19e shows a high density of dimples. A mixture of voids and dimples can be seen in Fig. 19f. The fracture surfaces of the 304L with reverse loading show dense and fine dimples arising from the grain refinement during the

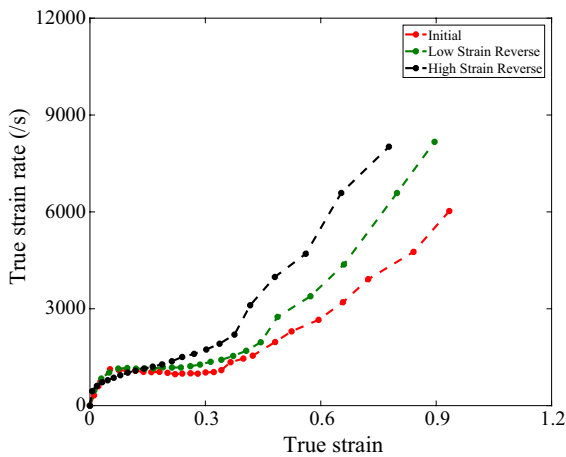


Fig. 16 Typical dynamic local strain rate evolution of the 304L without reverse loading, with LSR and HSR loading at nominal strain rate of 900–1110/s

reverse loading process [41, 42]. Likewise, these fracture surfaces of the 304L with reverse loading present a more homogeneous distribution of dimples, which coincide with the observations in the pre-strained and reverse loaded materials in Refs. [54, 57].

The fracture surfaces of the 304L with different loading conditions are shown in Fig. 20 at a higher level of magnification. Figure 20a, b show the elongated dimples are evenly distributed in the dynamically failed 304L without reverse loading and with

LSR loading. A high density of dimples exists in the dynamically failed 304L with HSR loading (Fig. 20c). Voids can be observed in the fracture surfaces in the 304L, regardless of the reverse loading history. This microstructural characterization section aims at illustrating that the 304L rods with three different loading conditions present ductile failure mode [55, 57]. This is consistent with the good impact energy absorption of the reverse loaded 304L.

4 Discussion

The materials and structures in the aircraft wing and jet engine containment system [31, 34, 58] would suffer from the impact loading. During the manufacturing process or in service, the unavoidable reverse loading would influence the mechanical properties of materials. Evaluations of the mechanical behavior and the energy absorption of materials with reverse loading history are important for a safe design. The metallic alloys, subjected to the tensile loading, experience inhomogeneous deformation and strain localization beyond a maximum force. Analysis of the materials under impact loading requires an understanding of the dynamic strain localization process. This work aims to study the effect of the reverse loading history on the subsequent dynamic strain localization and energy

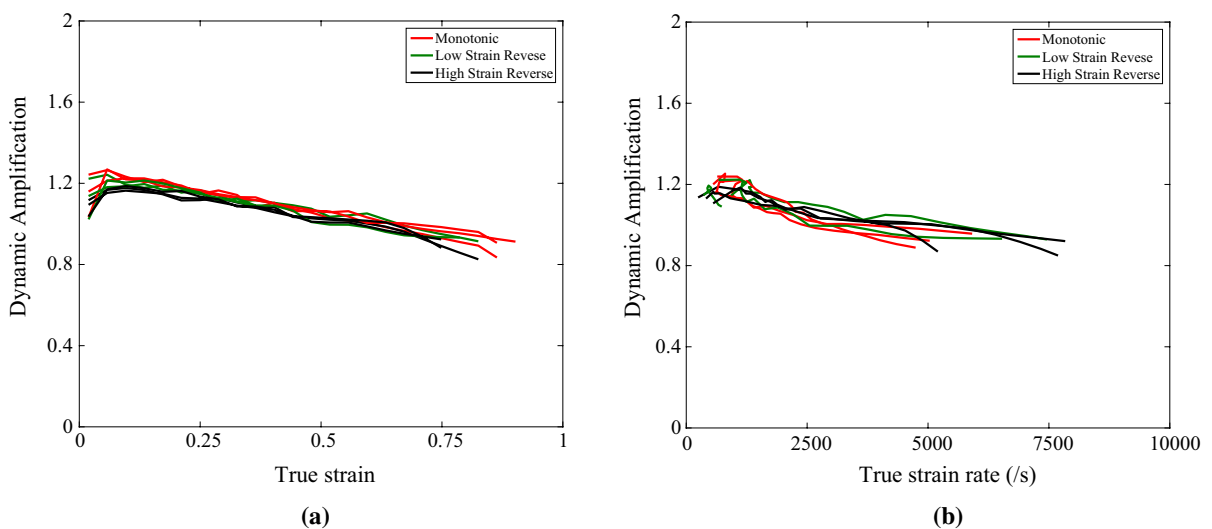


Fig. 17 Dynamic amplification as a function of **a** true strain and **b** true strain rate

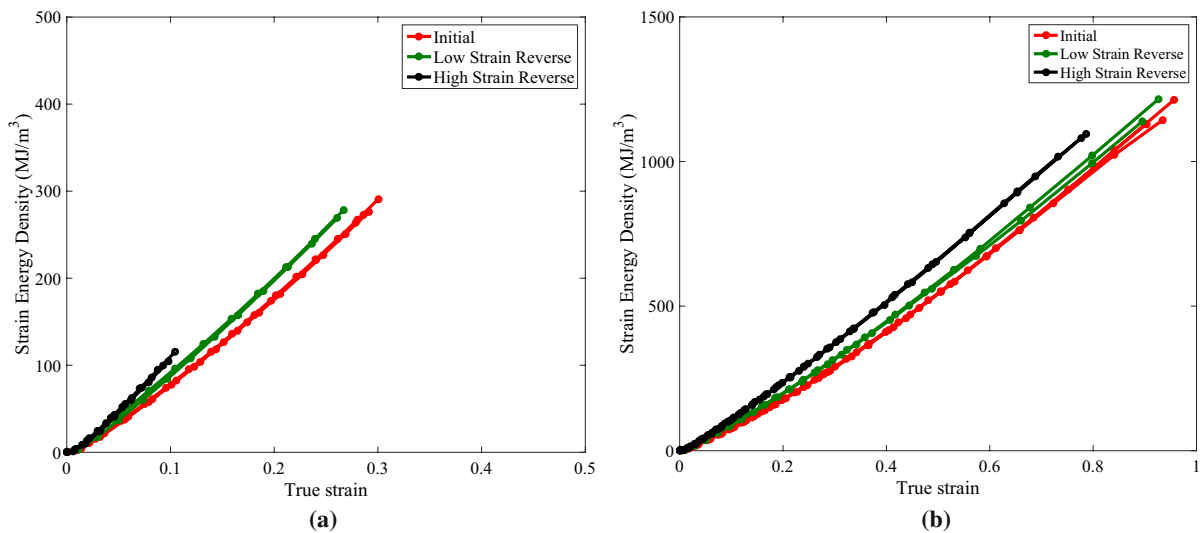


Fig. 18 Impact energy absorption of the 304L without reverse loading, with LSR and HSR loading **a** Energy absorption up to necking **b** Energy absorption up to fracture

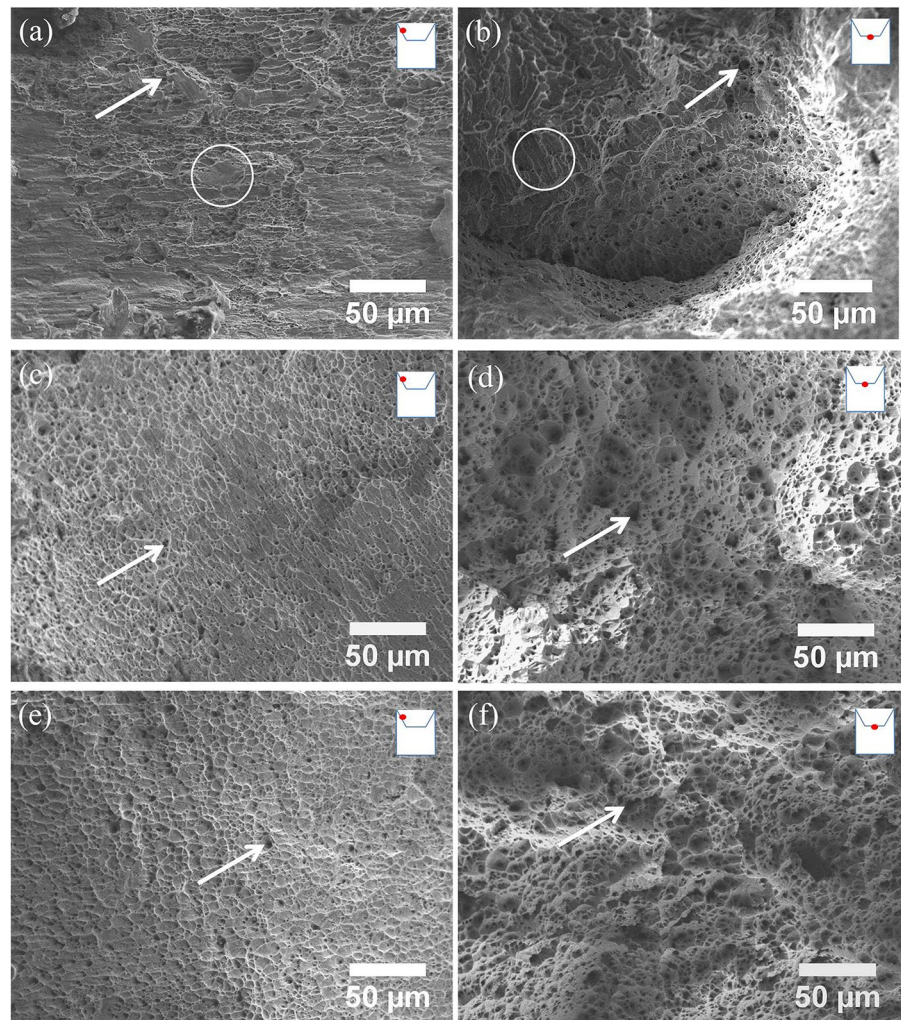
absorption of ductile rods, by using 304L as a model material due to its good ductility and its applications in aircraft structural components. The main results and discussions are given as follows.

A bespoke reverse loading setup is constructed in this work. This setup is based on the screw-driven Zwick Z50 machine and the Imetrum video extensometer system. The engineering strain of the specimen gauge section is monitored by the Imetrum system in real time. This provides feedback to the Zwick machine to apply the strain controlled reverse loading directly to the specimen gauge section. The dog-bone specimen with a 3 mm gauge length is proposed for the reverse loading tests. The stress–strain relation before necking is found to be independent of the specimen gauge length. The large strain reverse loading is difficult, due to the potential buckling of specimen at the compressive reverse loading stage [16]. Hence, the relatively short gauge length specimen is used in this work. With the bespoke reverse loading setup and the proposed specimen, the tension–compression reverse loading up to a strain of 0.16 was successfully conducted. The constitutive relationship measured by the Imetrum system agrees with that measured by the DIC. Here, only one cycle of tension–compression loading is applied to the specimen, in order to avoid the micro damages to the specimen [10, 14]. This enables the local true stress–strain relationship of the reverse loaded specimen to be measured, using the volume constancy.

With this bespoke setup, the Bauschinger effect of the 304L is characterized by a reduced yield stress at the beginning of reversal loading, as shown in Fig. 6. The reverse loading affects the interior microstructure [59, 60], see the detailed microstructural characterizations (such as martensitic transformation) of the 304 steel under reverse loading reported by Taleb et al. [61] and Hamasaki et al. [16] and Guo et al. [62]. The occurrence of the Bauschinger effect is mainly due to the back stress and the dislocation motion [50]. The 304L presents a permanent softening behavior and a significant Bauschinger effect [63] during the large strain reverse loading process. These agree with the results of Manninen et al. [15]. However, the available literature is limited to only one incomplete cycle of large strain reverse loading (the reverse compressive loading has to stop shortly after reaching the reverse yield stress), as the misalignment of the specimen prevent the compressive loading to continue.

The current setup allows the cycle of tension–compression loading to complete. After the reverse loading, the specimens are tested from quasi-static to high strain rates. The strain of the specimen gauge section is directly measured by the DIC technique. The 304L with high strain reverse loading shows significantly higher flow stress than that of the initial 304L. This is a result of grain refinement during the reverse loading [41, 42] and the Hall–Petch effect in the 304L material [42, 64, 65]. Although the plastic flow is greatly

Fig. 19 Fracture surfaces of the dynamically failed 304L **a, b** without reverse loading, **c, d** with LSR loading and **(e, f)** with HSR loading

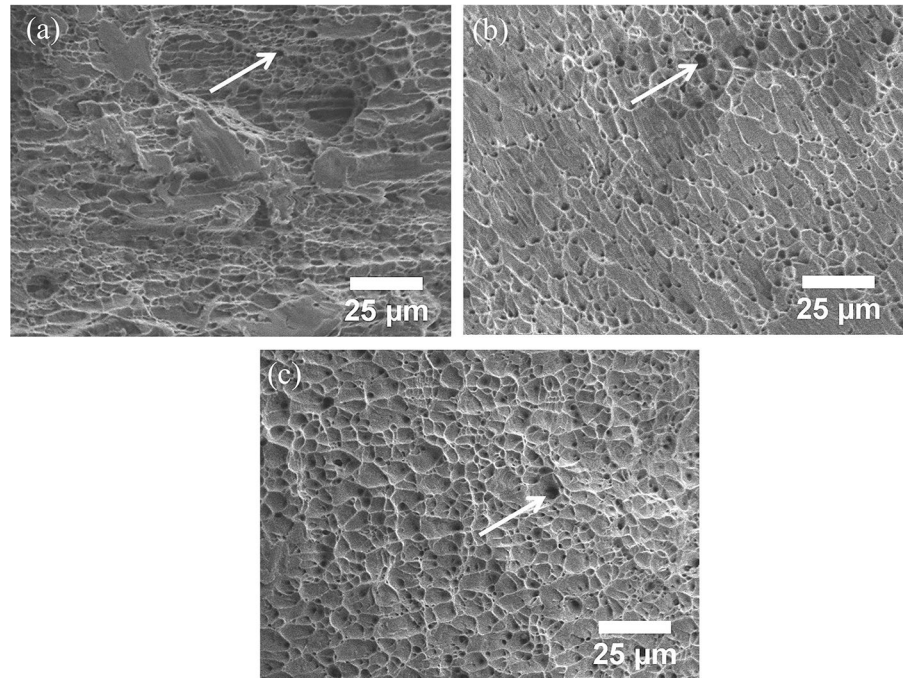


influenced by the reverse loading history, the strain rate sensitivity of the flow stress at the strain of 0.05 seems to be less affected by the reverse loading history, as shown in Fig. 14. The increasing trend of the initial flow stress as a function of strain rate is nonlinear, which can be predicted by the Cowper–Symonds model [52].

Dynamic strain localization of the 304L without and with reverse loading is monitored. The local strain rate of the reversed loaded 304L increases dramatically and becomes 10 times higher than the nominal strain rate. Given the evolution of local strain rate, the dynamic amplification factors over various local strain and local strain rate are evaluated. Contrary to the surge of local strain rate, the local stress does not show a dramatic increase. The dynamic flow

stress depends on the instantaneous strain rate and the strain rate history [66, 67]. Recently, Jacques and Rodríguez-Martínez [68] distinguished the instantaneous strain-rate sensitivity and the work-hardening strain-rate sensitivity in necking development. The effect of the work-hardening strain-rate sensitivity on the plastic flow depends on the current strain rate of the necking zone, and also the previous strain rate history. Likewise, dynamic necking is associated with thermal softening arising from the thermomechanical conversion [18, 69, 70]. The dynamic plastic flow is governed by working-hardening, strain rate and thermal softening. Consequently, the rapid increase of local strain rate would not immediately result in an increase in the flow stress and the dynamic amplification. These analyses agree with the recent

Fig. 20 Higher level magnification of the fracture surfaces of dynamically failed 304L, **a** without reverse loading, **b** with LSR loading and **c** with HSR loading



observations of Mirone et al. [40, 71, 72] in the Hopkinson bar tensile tests.

Analysis of the reverse loading effect on the impact energy absorption is of interest. Different from the evaluation of strain energy density up to necking in the work of Lopez and Verleysen et al. [14], this work studies the local stress–strain relation and the corresponding strain energy density up to the fracture. Due to the early necking (smaller strain to necking) of the 304L with reverse loading, the evaluation of the energy absorption up to necking would be misleading (Fig. 18a). Analysis of the local behavior shows that the energy absorption of the 304L with HSR loading is only slightly (about 5%) lower than the initial 304L and the 304L with LSR loading, as can be seen in Fig. 18b. Consequently, good impact energy absorption can be maintained in the reverse loaded 304L. This agrees with the characterized ductile fracture surfaces of the 304L with reverse loading history. The fracture surfaces of the initial 304L and the 304L with LSR loading show evenly distributed elongated dimples (Fig. 19a, c). The dynamically failed 304L with HSR loading shows a high density of dimples in Fig. 19e, which is attributed to the significant grain size refinement during the reverse loading [41, 42] and agrees with the fracture surface characterizations in Refs. [54, 57].

Compared to the reduced dynamic failure strain from the initial 304L to the 304L with HSR in Figs. 12 and 15, the impact energy absorption is found to be almost not influenced by the mechanical work during the cycle loading process. One can associate this result with the noticeable energy conception for dynamic shear failure proposed by Rittel et al. [73–75] in recent decades. Irrespective of the prestrain, the dynamic energy density up to failure remained quite constant [73]. The reduced extensional ductility of reversely pre-strained materials can be found in a number of early works of Swift [76], Nypan [77], Rockey [78] and Coffin [79]. The constant energy is suggested as a simple failure criterion of material with cyclic prestraining, which agrees with the Cockcroft–Latham criterion [80]. Consequently, the energy conception is of great importance to describe dynamic strain localization (necking and shear strain localization) of ductile materials.

Although the dynamic strain localization of the reverse loaded material is the main concern in this paper, the bespoke reverse loading setup can be extended to a number of works in the future, for instance, systematical studies of the Bauschinger effect and the corresponding microstructural evolutions, the flow and failure of advanced alloys

subjected to multi-cycles reverse loading. In addition, the tension–compression reverse loading or the compression–tension reverse loading can be applied to the specimen at different strain levels. The effect of fatigue damage on the flow and failure of engineering alloys can also be studied in the future. These will support the development of constitutive model of materials for engineering applications in the next step.

5 Conclusion

This work reports the dynamic strain localization of the 304L and its dependence on the large strain reverse loading history. Several bespoke techniques are used to characterize the responses of ductile 304L under large deformation. The main outcomes are summarized as follows:

- A bespoke reverse loading Zwick-Imetrum system is constructed, with real time strain control capability. This setup applies the reverse loading directly to the specimen gauge section up to a strain level of ± 0.16 . Likewise, this bespoke setup can be used to reveal the Bauschinger effect of the ductile materials.
- The development of necking instabilities is affected by the reverse loading history. The large strain reverse loading results in an early necking and the subsequent strain localization during most of the test duration.
- The local strain rate of the reverse loaded 304L increases dramatically during the dynamic strain localization. A higher strain reverse loading results in a higher local stress and a higher local strain rate.
- Analysis of the local stress–strain relationship shows the decrease of the dynamic amplification with the increase of local strain rate. This indicates the surge of local strain rate does not immediately result in an increase in the local stress.
- The effect of reverse loading should be considered to evaluate the impact energy absorbing capacities of the structural components. The 304L materials with reverse loading history show good crash energy absorption, which agrees with the microstructural characterizations with ductile failure mode.

Acknowledgements The assistance from Mrs. K. Bamford and Mr. S. Carter, the communications with Dr. HB. Yu at the Canadian Nuclear Laboratories, Dr. K. Dragnevski at the University of Oxford, Dr. DAS. Macdougall and Dr. J. Reed from Rolls-Royce pl are appreciated. Prof. N. Petrinic is acknowledged for the hunting equipment to break the steel. The insightful comments and suggestions from the anonymous reviewers are appreciated.

Author contributions LZ: Conceptualization, investigation, methodology, visualization, writing—original draft, writing—review and editing. DT: Resource, Investigation, Methodology, Writing—review and editing.

Declarations

Conflict of interest The authors declare that they have no known competing financial interests or personal relationships that could influence this work.

Open Access This article is licensed under a Creative Commons Attribution 4.0 International License, which permits use, sharing, adaptation, distribution and reproduction in any medium or format, as long as you give appropriate credit to the original author(s) and the source, provide a link to the Creative Commons licence, and indicate if changes were made. The images or other third party material in this article are included in the article's Creative Commons licence, unless indicated otherwise in a credit line to the material. If material is not included in the article's Creative Commons licence and your intended use is not permitted by statutory regulation or exceeds the permitted use, you will need to obtain permission directly from the copyright holder. To view a copy of this licence, visit <http://creativecommons.org/licenses/by/4.0/>.

Appendix A

To analyze the stress triaxiality distribution along the specimen gauge section, the finite element simulation is performed to evaluate the triaxiality factors along the specimen axis and a cylinder generatrix on the outer specimen surface. The simulation was performed using a commercial software ABAQUS. The pre-necking tensile stress–strain curve at strain rate of 0.01/s is used as input material data. The specimen is modelled as axisymmetric, and meshed with reduced integration element CAX4R. The element size of the gauge section is $0.1 \times 0.1 \text{ mm}^2$ with default hourglass control. Figure 21 shows that the stress triaxiality decreases from the end of gauge section to the center of gauge section. The stress triaxiality at most of the gauge section is between 0.29 and 0.39. The stress triaxiality at the center of gauge section is in the range of 0.33–0.34 at engineering strain of 0.16.

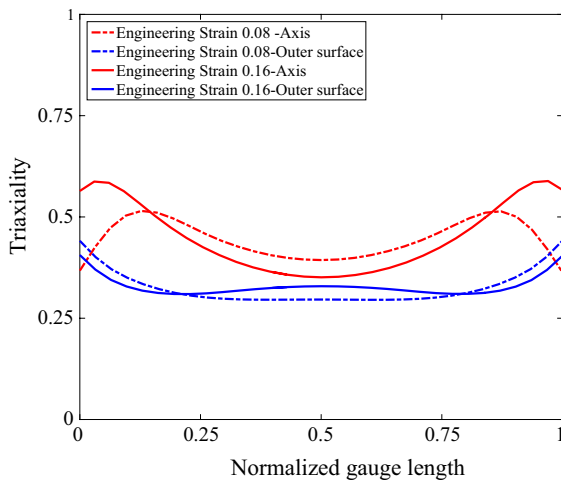


Fig. 21 Evaluation of stress triaxiality distribution of the proposed specimen subjected to tensile loading at engineering strain of 0.08 and 0.16

References

- Meyers MA (1994) Dynamic behavior of materials. Wiley
- Zhang T, Ma S, Zhao D, Wu Y, Zhang Y, Wang Z, Qiao J (2020) Simultaneous enhancement of strength and ductility in a NiCoCrFe high-entropy alloy upon dynamic tension: Micromechanism and constitutive modeling. *Int J Plast* 124:226–246
- Peroni L, Peroni M (2008) Development of testing systems for dynamic assessment of sheet metal specimens. *Meccanica* 43:225–236
- Rodríguez-Martínez J, Cazacu O, Chandola N, N'souglo KE (2021) Effect of the third invariant on the formation of necking instabilities in ductile plates subjected to plane strain tension. *Meccanica* 56:1789–1818
- Rittel D, Zhang L, Osovski S (2017) Mechanical characterization of impact-induced dynamically recrystallized nanophase. *Phys Rev Appl* 7:044012
- Pinnola FP, Zavarise G, Del Prete A, Franchi R (2018) On the appearance of fractional operators in non-linear stress–strain relation of metals. *Int J Non-Linear Mech* 105:1–8
- Franchi R, Del Prete A, Umbrello D (2017) Inverse analysis procedure to determine flow stress and friction data for finite element modeling of machining. *Int J Mater Form* 10:685–695
- Duyi Y, Zhenlin W (2001) Change characteristics of static mechanical property parameters and dislocation structures of 45# medium carbon structural steel during fatigue failure process. *Mater Sci Eng A* 297:54–61
- Sánchez-Santana U, Rubio-González C, Mesmacque G, Amrouche A, Decoopman X (2008) Effect of fatigue damage induced by cyclic plasticity on the dynamic tensile behavior of materials. *Int J Fatigue* 30:1708–1719
- Močko W, Brodecki A, Kruszka L (2016) Mechanical response of dual phase steel at quasi-static and dynamic tensile loadings after initial fatigue loading. *Mech Mater* 92:18–27
- Ye D (2005) Effect of cyclic straining at elevated-temperature on static mechanical properties, microstructures and fracture behavior of nickel-based superalloy GH4145/SQ. *Int J Fatigue* 27:1102–1114
- Froustey C, Lataillade JL (2009) Influence of the microstructure of aluminium alloys on their residual impact properties after a fatigue loading program. *Mater Sci Eng A* 500:155–163
- Froustey C, Auzanneau T, Charles J-L, Lataillade J-L (2000) Fatigue acceptable damage threshold and fatigue failure threshold according to a residual impact behaviour of an aluminium alloy. *Le J Phys IV* 10:Pr9-565-Pr569-570
- Lopez J, Verleysen P, Degrieck J (2012) Effect of fatigue damage on static and dynamic tensile behaviour of electro-discharge machined Ti-6Al-4V. *Fatigue Fract Eng Mater Struct* 35:1120–1132
- Manninen T, Myllykoski P, Taulavuori T, Korhonen A (2009) Large-strain Bauschinger effect in austenitic stainless steel sheet. *Mater Sci Eng A* 499:333–336
- Hamasaki H, Ohno T, Nakano T, Ishimaru E (2018) Modelling of cyclic plasticity and martensitic transformation for type 304 austenitic stainless steel. *Int J Mech Sci* 146:536–543
- Considère M (1885) Memoire sur l'emploi du fer et de l'acier dans les constructions. Dunod
- Rittel D, Zhang LH, Osovski S (2017) The dependence of the Taylor-Quinney coefficient on the dynamic loading mode. *J Mech Phys Solids* 107:96–114
- Sancho A, Cox MJ, Cartwright T, Davies CM, Hooper PA, Dear JP (2019) An experimental methodology to characterise post-necking behaviour and quantify ductile damage accumulation in isotropic materials. *Int J Solids Struct* (176-177):191–206
- Vaz-Romero A, Rotbaum Y, Rodríguez-Martínez J, Rittel D (2016) Necking evolution in dynamically stretched bars: New experimental and computational insights. *J Mech Phys Solids* 91:216–239
- Mirone G, Barbagallo R, Tedesco MM, De Caro D, Ferreira M (2022) Extended stress-strain characterization of automotive steels at dynamic rates. *Metals* 12:960
- Harding J, Wood E, Campbell J (1960) Tensile testing of materials at impact rates of strain. *J Mech Eng Sci* 2:88–96
- Harding J (1965) Tensile impact testing by a magnetic loading technique. *J Mech Eng Sci* 7:163–176
- Noble J, Goldthorpe B, Church P, Harding J (1999) The use of the Hopkinson bar to validate constitutive relations at high rates of strain. *J Mech Phys Solids* 47:1187–1206
- Mirone G, Corallo D, Barbagallo R (2017) Experimental issues in tensile Hopkinson bar testing and a model of dynamic hardening. *Int J Impact Eng* 103:180–194
- Mirone G, Barbagallo R, Giudice F, Di Bella S (2020) Analysis and modelling of tensile and torsional behaviour at different strain rates of Ti6Al4V alloy additive

- manufactured by electron beam melting (EBM). *Mater Sci Eng A* 793:139916
27. Cadoni E, Forni D (2019) Austenitic stainless steel under extreme combined conditions of loading and temperature. *J Dyn Behav Mater* 5:230–240
 28. Guo B, Xie H, Zhu J, Wang H, Chen P, Zhang Q (2011) Study on the mechanical behavior of adhesive interface by digital image correlation. *Sci China Phys Mech Astron* 54:574–580
 29. Arora H, Hooper PA, Dear JP (2011) Dynamic response of full-scale sandwich composite structures subject to air-blast loading. *Compos A Appl Sci Manuf* 42:1651–1662
 30. Rose L, Menzel A (2021) Identification of thermal material parameters for thermo-mechanically coupled material models. *Meccanica* 56:393–416
 31. Rolls-Royce plc (2015) *The jet engine*. Wiley
 32. Sinha SK, Dorbala S (2009) Dynamic loads in the fan containment structure of a turbofan engine. *J Aeronaut Eng* 22:260–269
 33. Naik D, Sankaran S, Mobasher B, Rajan S, Pereira J (2009) Development of reliable modeling methodologies for fan blade out containment analysis—Part I: experimental studies. *Int J Impact Eng* 36:1–11
 34. Carney K, Pereira JM, Revilock D, Matheny P (2009) Jet engine fan blade containment using an alternate geometry. *Int J Impact Eng* 36:720–728
 35. Lee W-S, Lin C-F (2002) Comparative study of the impact response and microstructure of 304L stainless steel with and without prestrain. *Metall Mater Trans A* 33:2801–2810
 36. Lee W-S, Lin C-F (2001) Impact properties and microstructure evolution of 304L stainless steel. *Mater Sci Eng A* 308:124–135
 37. Rao KBS, Valsan M, Sandhya R, Mannan S, Rodriguez P (1993) An assessment of cold work effects on strain-controlled low-cycle fatigue behavior of type 304 stainless steel. *Metall Trans A* 24:913–924
 38. Iino Y (1992) Effect of small and large amounts of pre-strain at 295K on tensile properties at 77K of 304 stainless steel. *JSME Int J. Ser 1 Solid Mech Strength Mater* 35:303–309
 39. Bridgman PW (1952) *Studies in large plastic flow and fracture*. McGraw-Hill New York, New York
 40. Miron G, Barbagallo R, Giudice F (2019) Locking of the strain rate effect in Hopkinson bar testing of a mild steel. *Int J Impact Eng* 130:97–112
 41. Järvenpää A, Jaskari M, Man J, Karjalainen LP (2017) Stability of grain-refined reversed structures in a 301LN austenitic stainless steel under cyclic loading. *Mater Sci Eng A* 703:280–292
 42. Kumar SS, Vasanth M, Singh V, Ghosal P, Raghu T (2017) An investigation of microstructural evolution in 304L austenitic stainless steel warm deformed by cyclic channel die compression. *J Alloy Compd* 699:1036–1048
 43. López JG, Verleysen P, De Baere I, Degrieck J (2011) Tensile properties of thin-sheet metals after cyclic damage. *Procedia Eng* 10:1961–1966
 44. Zhang C, Wang R, Song G (2020) Effects of pre-fatigue damage on mechanical properties of Q690 high-strength steel. *Constr Build Mater* 252:118845
 45. Močko W, Brodecki A, Radziejewska J (2015) Effects of pre-fatigue on the strain localization during tensile tests of DP 500 steel at low and high strain rates. *J Strain Anal Eng Des* 50:571–583
 46. Gerlach R, Kettenbeil C, Petrinic N (2012) A new split Hopkinson tensile bar design. *Int J Impact Eng* 50:63–67
 47. Gerlach R, Sathianathan SK, Siviour C, Petrinic N (2011) A novel method for pulse shaping of Split Hopkinson tensile bar signals. *Int J Impact Eng* 38:976–980
 48. Meyers MA, Chawla KK (2008) *Mechanical behavior of materials*. Cambridge University Press
 49. Bauschinger J (1881) Ueber die Veränderung der Elasticitätsgrenze und elasticitätsmodul verschiedener. *Metal Civiling N.F.* 27:289–348
 50. Abel A, Muir H (1972) The Bauschinger effect and discontinuous yielding. *Phil Mag* 26:489–504
 51. Hopperstad O, Børvik T, Langseth M, Labibes K, Albertini C (2003) On the influence of stress triaxiality and strain rate on the behaviour of a structural steel: part I. *Exp Eur J Mech A/Solids* 22:1–13
 52. Cowper GR, Symonds PS (1957) *Brown Univ. Tech. Rept. No. 28*
 53. Miron G, Corallo D, Barbagallo R (2016) Interaction of strain rate and necking on the stress-strain response of uniaxial tension tests by Hopkinson bar. *Procedia Struct Integr* 2:974–985
 54. Dong Y, Sun Z, Xia H, Feng J, Du J, Fang W, Liu B, Wang G, Li L, Zhang X (2018) The influence of warm rolling reduction on microstructure evolution, tensile deformation mechanism and mechanical properties of an Fe-30Mn-4Si-2Al TRIP/TWIP steel. *Metals* 8:742
 55. Pantazopoulos GA (2019) A short review on fracture mechanisms of mechanical components operated under industrial process conditions: Fractographic analysis and selected prevention strategies. *Metals* 9:148
 56. Jelani M, Li Z, Shen Z, Hassan NU, Sardar M (2018) Mechanical response and failure evolution of 304L stainless steel under the combined action of mechanical loading and laser heating. *Metals* 8:620
 57. Peng J, Li K, Peng J, Pei J, Zhou C (2018) The effect of pre-strain on tensile behaviour of 316L austenitic stainless steel. *Mater Sci Technol* 34:547–560
 58. Gálvez F, Cendón D, Enfedaque A, Sánchez-Gálvez V (2006) High strain rate and high temperature behaviour of metallic materials for jet engine turbine containment. *J Phys IV* 134:269–2746
 59. Hilditch TB, Timokhina IB, Robertson LT, Pereloma EV, Hodgson PD (2009) Cyclic deformation of advanced high-strength steels: mechanical behavior and microstructural analysis. *Metall Mater Trans A* 40:342–353
 60. Stephens RI, Fatemi A, Stephens RR, Fuchs HO (2000) *Metal fatigue in engineering*. Wiley
 61. Taleb L, Hauet A (2009) Multiscale experimental investigations about the cyclic behavior of the 304L SS. *Int J Plast* 25:1359–1385
 62. Guo N, Zhang Z, Dong Q, Yu H, Song B, Chai L, Liu C, Yao Z, Daymond MR (2018) Strengthening and toughening austenitic steel by introducing gradient martensite via cyclic forward/reverse torsion. *Mater Des* 143:150–159
 63. Como M, D'Agostino S (1969) Strain hardening plasticity with bauschinger effect. *Meccanica* 4:146–158

64. Hansen N (2004) Hall-Petch relation and boundary strengthening. *Scr Mater* 51:801–806
65. Qu S, Huang C, Gao Y, Yang G, Wu S, Zang Q, Zhang Z (2008) Tensile and compressive properties of AISI 304L stainless steel subjected to equal channel angular pressing. *Mater Sci Eng A* 475:207–216
66. Nicholas T (1971) Strain-rate and strain-rate-history effects in several metals in torsion. *Exp Mech* 11:370–374
67. Campbell J, Eleiche A, Tsao M (1977) Strength of metals and alloys at high strains and strain rates. *Fundamental aspects of structural alloy design*. Springer, Boston, pp 545–563
68. Jacques N, Rodríguez-Martínez J (2021) Influence on strain-rate history effects on the development of necking instabilities under dynamic loading conditions. *Int J Solids Struct* 230:111152
69. Nieto-Fuentes J, Osovski S, Venkert A, Rittel D (2019) Reassessment of the dynamic thermomechanical conversion in metals. *Phys Rev Lett* 123:255502
70. Zaera R, Rodríguez-Martínez JA, Rittel D (2013) On the Taylor-Quinney coefficient in dynamically phase transforming materials: application to 304 stainless steel. *Int J Plast* 40:185–201
71. Mirone G (2013) The dynamic effect of necking in Hopkinson bar tension tests. *Mech Mater* 58:84–96
72. Mirone G, Barbagallo R (2021) EPJ Web of Conferences, EDP Sciences,.
73. Rittel D, Wang Z, Merzer M (2006) Adiabatic shear failure and dynamic stored energy of cold work. *Phys Rev Lett* 96:075502
74. Dolinski M, Rittel D, Dorogoy A (2010) Modeling adiabatic shear failure from energy considerations. *J Mech Phys Solids* 58:1759–1775
75. Dolinski M, Merzer M, Rittel D (2015) Analytical formulation of a criterion for adiabatic shear failure. *Int J Impact Eng* 85:20–26
76. Swift HW (1939) Tensional effects of torsional overstrain in mild steel. *J Iron Steel Inst* 140:181
77. Nypan L (1971) Effect of unidirectional and reversed torsion on the strength and ductility of 2024 aluminium. *J Strain Anal* 6:25–26
78. Rockey K (1967) The influence of large torsional strains upon the subsequent extensional behaviour of a low carbon steel. *Int J Mech Sci* 9:767–774
79. Coffin LF Jr (1954) A study of the effects of cyclic thermal stresses on a ductile metal. *Trans Am Soc Mech Eng* 76:931–949
80. Cockcroft M (1968) Ductility and workability of metals. *J Metals* 96:2444

Publisher's Note Springer Nature remains neutral with regard to jurisdictional claims in published maps and institutional affiliations.